Extinction of light and coherent scattering by a single nitrogen-vacancy center in diamond

Thai Hien Tran,[1] Petr Siyushev,[1,*] Jörg Wrachtrup,[1,2] and Ilja Gerhardt[1,2,†]

[1]*3rd Institute of Physics, University of Stuttgart, and Center for Integrated Quantum Science and Technology (IQST), Pfaffenwaldring 57, D-70569 Stuttgart, Germany*

[2]*Max Planck Institute for Solid State Research, Heisenbergstraße 1, D-70569 Stuttgart, Germany*

(Received 17 August 2016; published 10 May 2017)

The efficient interaction of light and a single quantum system is required to implement a photon to spin interface. It is important to determine the amount of coherent and incoherent photons in such a scheme, since it is based on coherent scattering. In this paper an external laser field is efficiently coupled to a single nitrogen vacancy center in diamond. We detect the direct extinction signal and estimate the nitrogen vacancy's extinction cross section. The exact amount of coherent and incoherent photons is determined against the saturation parameter. This reveals the optimal point of interaction for further experiments. A theoretical model allows us to explain the deviation to an atom in free space. The introduced experimental techniques are used to determine the properties of the tight focusing in an interference experiment and allow for a direct determination of the Gouy phase in a strongly focused beam.

DOI: 10.1103/PhysRevA.95.053831

I. INTRODUCTION

The nitrogen vacancy (NV) center in diamond allows for quantum sensing [1,2], and a variety of quantum optical primitives. These cover the single-shot readout of a nuclear spin [3], quantum error correction [4], and the coupling of neighboring defects [5]. While the described experiments rely on an optical readout of the electron (and eventually the accessible nuclear) spin, another line of experiments deals with the *distant* interaction of NV centers by means of optical photons [6]. This requires cryogenic conditions, and only 3%–4% of all emitted photons are used [7,8]. All experiments up to now have relied on a remote photon-photon interaction, rendering the systems in an entangled state, and Bell's inequality is violated [9,10]. Unfortunately, this implies the coincidental detection of two indistuinguishable photons from two remote NV centers, which limits the achievable entanglement rates. The direct means of optical interaction, namely, the emission of a photon by one quantum system and the excitation of another, has not been realized so far. This requires coherent scattering, which allows for excitation of the receiving quantum system.

The theory of coherent scattering of a single emitter has been established since the 1960s [12,13]. Early experiments on atoms or ions showed the expected behavior of a two-level system [14,15]. Spectroscopy on solid-state emitters, such as molecules and quantum dots, involves more effects on the amount of coherent scattering, such as phonon contributions. Recent progress has shifted the focus in single-emitter spectroscopy from a high *collection efficiency* to an *efficient coupling* of an external field towards an emitter. In the past decade such measurements have been performed [16–19], and they allow for ultranarrow-band photons [20] and enable squeezing measurements on the light of single emitters [21].

To allow for the estimation of a remote optical interaction in a sender-receiver configuration, we perform a measurement of the coherent scattering of a single NV center. This is monitored by the direct extinction of light by the nanoscopic emitter. *Direct* refers in this context to a simple observation of an altered laser with a single-photon detector [22]. The amount of coherent and incoherent scattered photons changes with the incident flux of photons [23]. The measurements reveal directly the achievable interaction in a receiving quantum node and allow estimation of the best interaction mechanism. An interferometric application of this atom-sized defect is applied to a measurement of the Gouy phase in the tight laser focus.

The extinction of light by a single emitter is one of the most evident proofs of coherent scattering [15,22]. Usually, an incoming laser beam is altered by the presence of an emitter in the optical path. The amount of light, collected on a detector in the forward direction, is given as $I_{\mathrm{det}} = \langle(\mathbf{E}_{\mathrm{laser}} + \mathbf{E}_{\mathrm{emitter}})^2\rangle$, i.e., the incident laser light and the coherently scattered light interfere destructively in the optical far field. This is commonly described as *extinction*. In the case of a purely coherently scattering emitter, such as an atom at the low excitation limit, the light is reflected back to the exciting laser [24] and the light in the forward direction is perfectly extinguished. This allows for quantum-state transfer of the incoming photon into the receiving quantum node.

Extinction measurements can be performed not just in the forward direction [22]. Generally, the interference occurs in all directions, but as outlined in the optical theorem [25] the extinction in the forward and the backward direction amounts to the same value as the *absorption*, which is the transfer to other forms of energy, such as heat. If parts of the laser light are reflected elsewhere, or coupled deliberately onto the detector, the resulting interference signal can have an arbitrary phase, φ, depending on the relative phase of the reflected light to the coherent scattering of the emitter. For an emitter with a lifetime-limited line it is possible to rewrite the above equation and describe the signal on the detector as

$$I_{\mathrm{det}} = I_{\mathrm{laser}}\left(1 - \mathcal{V}\frac{\Gamma_2(\Delta\cos\varphi + \Gamma_2\sin\varphi)}{\Delta^2 + \Gamma_{\mathrm{eff}}^2}\right), \qquad (1)$$

*Present address: Institute for Quantum Optics, University Ulm, Albert-Einstein-Allee 11, 89081 Ulm, Germany.

†i.gerhardt@fkf.mpg.de

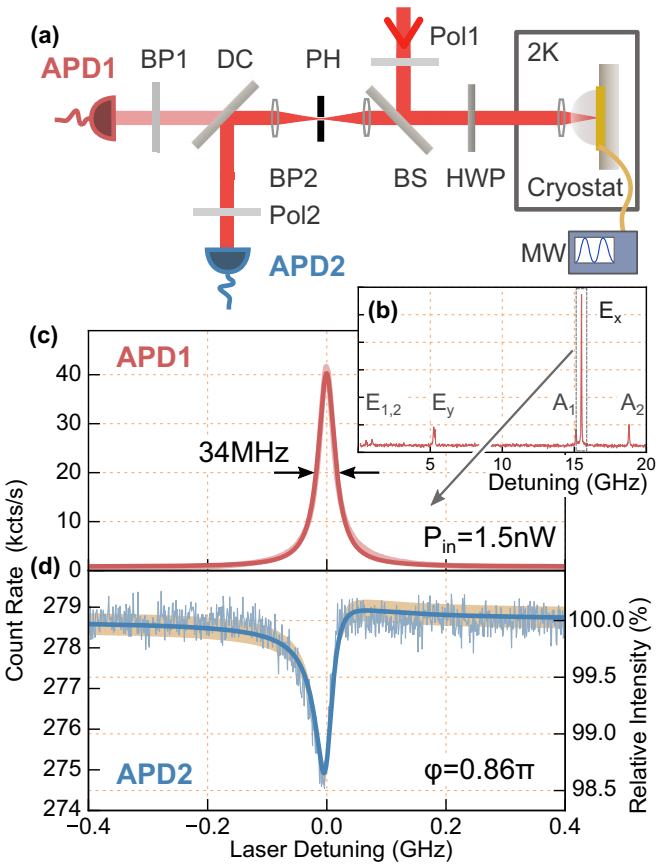

FIG. 1. (a) The experimental setup consists of a cryogenic confocal microscope. Two detection arms analyze the emission of the photon side band (APD1) and the coherent laser light (APD2) (b) Fluorescence excitation spectrum behind a 650- to 750-nm band-pass filter (BP1) [11]. (c) Zoom-in on the E_x transition. (d) Coherent scattering of the NV and its interference with the incoming laser. DC, dichroic; HWP, half-wave plate; MW, microwave; PH, pinhole; Pol, polarizer.

with a reflected flux of the laser of I_{laser}, visibility $\mathcal{V}$, homogeneous linewidth $2\Gamma_2$, effective, e.g., power-broadened, linewidth $2\Gamma_{\text{eff}}$, and spectral detuning Δ. The *effective* visibility, or contrast, reduces with increasing excitation power expressed in the saturation parameter S as

$$\mathcal{C}(S) = \mathcal{V}\frac{1}{S+1}. \tag{2}$$

This measurable contrast, $\mathcal{C}$, is described by the fraction of missing light. It depends on the orientation of the emitter against the laser field, the amount of coherent vs incoherent scattering, the amount of collected light from the emitter and the laser, and other diminishing factors, such as the Debye-Waller factor α_{DW}. With a single NV center, only a small fraction of the emission [7] leads to interference due to the low spectral coherence of the emitted photons. This diminishes the effective extinction cross section, σ, to a fraction of the maximal theoretical possible value of $3\lambda^2/(2\pi)$, and extinction experiments with NV centers are hard and commonly require balanced detection or lock-in techniques [26].

Figure 1(a) shows the experimental setup. A tunable narrow-band laser (New-Focus Velocity; ≈637 nm) excites a single NV center inside a bath cryostat ($T = 2$ K). Tight focusing is realized by a microscope objective (Zeiss A-Plan; 40 ×, 0.65 NA) in conjunction with a hemispherical macroscopic ($\phi = 1$ mm) monolithic diamond solid-immersion lens (SIL; Element Six). It exhibits a 0.6-mm-thick overgrown layer of ultrapure diamond on the flat side. This contains single natural NV centers [27] suitable for cryogenic experiments. The polarization of the laser is laterally aligned with the E_x transition [Fig. 1(b)]. The spectral line manifold [E_x, etc.; see Fig. 1(a)] is named after the irreducible representations of the excited-state orbital ^{3}E [11,28].

Due to strain-induced mixing of the excited-state spin sublevels, optical excitation might introduce a spin flip. Since the optical transitions are spin selective, these reduce the excitation efficiency. This is avoided by applying a microwave field ($\nu = 2.87$ GHz) to keep the desired spin state always accessible. Resonant excitation might induce a two-photon process, leading to an ionization of the NV center into the neutral charge state [29]. If no fluorescence is observed in a frequency scan, a 300-ms green, 20-μW, 532-nm laser pulse is applied.

The emission of the phonon side band (PSB) is captured on a single-photon detector (APD1) behind a band-pass filter (650–750 nm). The laser back-scattering and zero-phonon line (ZPL) are captured on another single-photon detector (APD2). This light is reflected off a dichroic (Chroma ZT640) and passes a narrow-band filter (637 ± 1 nm; Omega Optical). The polarizer (Pol2) is aligned with the incident laser field. Both detectors' count rates are monitored against detuning of the excitation laser.

Figures 1(b) and 1(c) show the red-shifted emission from the NV center versus the laser detuning. Figure 1(c) is assembled of 2000 single spectra (each consisting of 1000 frequency pixels, which are each 2 ms long), shifted to their spectral center to suppress spectral diffusion, which spans a few hundred MHz. This is determined by fitting a Lorentzian to each of the lines. The resulting spectral linewidth (34 MHz) at 1.5-nW laser excitation (measured in front of the cryostat) shows that we exceed the lifetime-limited linewidth of $\Gamma_1 = 1/(2\pi T_1) \approx$ 13 MHz.

Simultaneously, the extinction of light is monitored on APD2 [Fig. 1(d)]. Far off-resonance, the signal is given by laser reflection mainly from the flat side of the SIL. Power fluctuations are suppressed to the shot-noise limit by a PID controller (SRS; PID960) in the excitation arm. When the laser is detuned and the emitter is on resonance, an extinction signal is observed as described by Eq. (1). Note that the detection pinhole (50 μm) is aligned such that the emission of the NV center is fully captured, whereas the laser reflection is (partially) out of focus and suppressed by 10^3.

The final phase φ of 0.86π to the exciting laser results from the depth of the emitter d, the refractive index n as $\varphi_d = \pi - 2\pi(2dn \bmod \lambda)$, and the phase difference of the laser reflection on all interfaces. If no surfaces and reflection are present, a Lorentzian reflection of the coherent scattering is observed [24]. The dominant noise source is shot noise [orange curve; Fig. 1(c); $\pm 1\,\sigma$]. The spectra are corrected from an internal cavity resulting from the cryostat windows. A signal-to-noise ratio (SNR) of 15 is observed. These experiments were also performed at the low excitation

limit (not shown). Correspondingly, the measured contrast is increased as $1/(S+1)$, with S being the saturation parameter on resonance $\Omega^2/(\Gamma_1\Gamma_2)$ [23], which depends on the excitation power Ω^2. Subsequently, a maximal contrast $\mathcal{C}$ of 2.8% is measured at the lower excitation limit, and $\mathcal{C}$ is equal to $\mathcal{V}$.

The observed signal on APD2 consists not only of the laser reflected from the interfaces and the coherent scattering of the NV center. It might contain a small amount of red-shifted fluorescence, which is present when the NV center is on resonance. This cannot interfere with the incident laser light. Therefore, all extinction measurements such as Fig. 1(d) contain both contributions. A full procedure to derive both components independently with the use of a polarizer [17] is described in the Appendix. Note that under close-to-crossed polarizer conditions, the contrast rises well above 5%.

As the extinction signal, the amount of coherent and incoherent scattering is power dependent on the saturation parameter S. This unitless entity influences the linewidth in the red-shifted fluorescence of the NV center on APD1 [Fig. 2(a); red circles]. The curve (red line) is fitted as $\Gamma_{\text{eff}} = \Gamma_2\sqrt{\frac{I_{\text{sat}}}{I_{\text{sat}}-I}}$ and allows us to determine I_{sat} and Γ_2. I_{sat} then reveals the saturation parameter $S = \frac{I}{I_{\text{sat}}-I}$ for the following measurements.

Figure 2(a) (red line) represents one measurement as in Fig. 1(c). The excitation power ranges from 0.3 to 3.0 nW (saturation parameter, up to 1.0). Due to the low SNR of the single scans at very low incident powers ($P_{\text{in}} <$ nW, APD2 $<$ 1.5 kcts/s), the fit error is increased and leads to an uncertainty in the fitted linewidth. The same holds for very high excitation powers, where the NV's spectral diffusion and the probability of ionization is increased. Since the measurement expands over several cooling cycles, cavity and thermal effects change the coupling and collection efficiency slightly. Therefore, we decided to use the PSB intensity as an indirect reference for the saturation parameter instead of the incoming power. The relationship between the laser power and the PSB intensity is independently validated by recording a saturation curve.

The contrast of the extinction signal is simultaneously recorded on APD2 [Fig. 2(a); blue diamonds]. This depends on the amount of coherently scattered photons. With increasing excitation power it is reduced as $1/(S+1)$. See the Appendix for details.

The experimentally determined amount of coherent scattering by the single NV center is displayed in Fig. 2(b) (blue diamonds). For a two-level system, with a collection efficiency of η, the amount of coherent scattering obeys the equation $I_{\text{coh}} = \eta\alpha_{\text{DW}}\frac{\Gamma_1^2}{4\Gamma_2}\frac{S}{(1+S)^2}$ [Fig. 2(b); gray line]. It implies that the amount of coherent scattering is highest at $S = 1$. Instead, we find the amount of coherent scattering reduced compared to its predicted value. This is expected since residual charge noise in the environment of the NV center increases exponentially with the excitation power as $\exp(-P_{\text{in}}/P_{\text{env}})$. With this model [solid blue curve in Fig. 2(b)], assuming that $P_{\text{env}} = 4.0$ nW, the amount of coherent photons is described well. Simultaneously, the incoherent scattering is monitored (red curve).

The optimal point at which to extract coherent photons corresponds to a saturation parameter of 0.45. In our experimental configuration this corresponds to 1.5 nW in front of the cryostat. This is the point where the highest ratio of coherent scattering vs incident light intensity is observed. This point should be determined for all experiments which utilize coherent photons or determine an optimal interaction. Figure 2(c) shows the ratio of coherent-to-incoherent scattering, while the description above gives the absolute range. Theoretically this obeys the factor $1/(1+S)$, but it is modified here due to charge noise from the environment as $\exp(-P_{\text{in}}/P_{\text{env}})/(1+S)$.

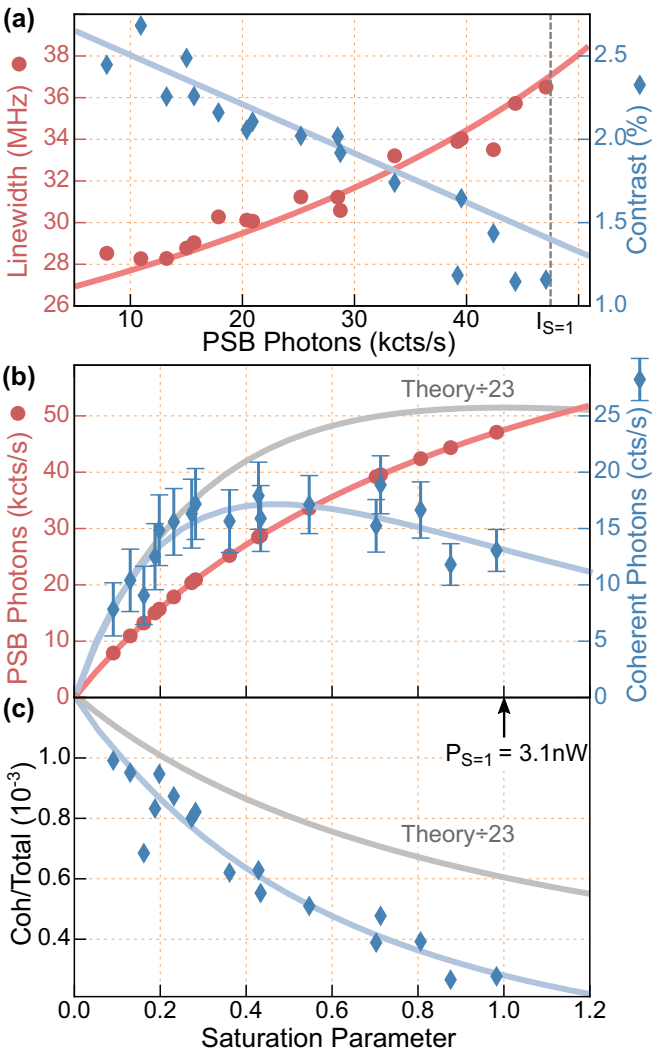

FIG. 2. (a) Determination of the saturation parameter by the linewidth measured on APD1 (red symbols). Contrast, measured on APD2, fitted by Eq. (1). The dashed line indicates the saturation intensity I_{sat}. (b) Amount of coherent (blue symbols) and PSB (red symbols) photons, as deduced from the data in (a). (c) Ratio of coherent photons to total emission. (b, c) Gray curves: theoretical amount and ratio of coherent photons calculated from the total collected PSB emission.

The extinction cross section σ_{ext} influences the contrast as σ_{ext}/A with the focal area A. The full set of experiments is used to deduce the extinction cross section of the NV center. It depends on various factors, such as the Debye-Waller factor (3%–4%), and the NV's physical orientation. The latter is deduced from the orientation of the diamond lattice and

the incident laser polarization. With the achievable extinction signal and its saturation behavior, we determine the extinction cross section as $\varnothing = 30\,\mathrm{nm}$. This value is now estimated for an experiment in the forward direction, such that the entire light beam would be captured by a single-photon detector. This value is strongly polarization dependent as $\cos(\theta)^2$, with θ the relative angle between the NV axis (with E_x being a linear dipole) and the laser. Therefore, it will be possible to influence an ongoing laser beam with the NV's spin state, e.g., on the A_1 or the A_2 transition. The achievable effect amounts to 2.3% (see Appendix). Of course, the measurable contrast can be artificially enhanced, by neglecting photons in the forward direction, e.g., in a crossed polarization configuration [16,26].

At the low excitation limit the probability of photons exciting the system is low. This implies that photons may be coherently scattered without subsequent excitation of the system. Quantum optical primitives, such as quantum nondemolition measurements, can be realized with this effect. Another option is interferometric applications with an atomic size defect: The Gouy phase $\phi(z)$ describes the "inversion" of the wave fronts in an optical focus [30,31]. This characterization of an optical focus with an atomic-sized defect was proposed in 2007 by Hwang and Moerner [32].

When the emitter is placed in the focused laser [Fig. 3(a)], with z_e as the axial position relative to the laser focus, the Gouy phase is observed by the change in the phase of the interferometric signal [32]. The phase difference between $z_e = -\infty$ and $z_e = +\infty$ is the total Gouy phase shift π, and its highest gradient is at the focus.

To measure the Gouy phase, the NV center is axially moved through the focus of the confocal microscope. By an earlier lateral scan [see Fig. 3(b)], a focus waist w_0 of $0.23 \pm 0.05\,\mu\mathrm{m}$ was estimated. This corresponds to a Rayleigh length z_R of $0.62^{+0.30}_{-0.24}\,\mu\mathrm{m}$. The Gouy phase is measured in a range of $\pm 2.5\,z_R$, corresponding to an expected change of $\Delta\varphi \approx 0.8\pi$. The excitation power is adjusted so that far in front and behind the focus the count rates are not dramatically reduced. The intensity distribution (i.e., power per area) is monitored along with the interferometric detection. The count rates, measured on APD1, normalized to the excitation intensity in the focus, are depicted in Fig. 3(c) (red symbols).

Simultaneously, the extinction of light is monitored on APD2. The phase φ reveals directly the information on the Gouy phase. Sample measurements are shown in Fig. 3(c) (Fig. 1 is in focus). The only fit parameters are the residual phase offset ($0.86\,\pi$ in the focus) and the collection efficiency, since all other parameters (z_R, w_0) are determined independently. The shaded band in the background indicates the error bar for estimating the Rayleigh length, z_R, as outlined above.

The presented measurements prove the ability to influence a laser field with an atomic-sized single quantum emitter and reach up to 2.8% direct influence on a back-reflected laser. The achievable effect will be higher when the polarizations of the excitation and detection are not aligned as in the present experiment. For the forward direction, the effect will be 0.42%, and every 250th photon interacts with the emitter. This allows an alternative way to mediate a remote spin-photon-spin interaction. Comparable experiments allow us to implement a variety of quantum optical primitives, such as a spin-dependent phase gate. Another possibility is quantum nondemolition experiments, which hold the promise of producing larger cluster states of light [33], or implementation of other schemes in quantum computing [34]. In the context of precision measurements, we like to emphasize that the described visibility is accessible under extremely low incident flux. For the low excitation limit this can exceed the SNR of fluorescence detection [17,35]. The first measurement reveals an interferometric measurement of the Gouy phase with an NV center. This compares to earlier single-ion experiments [36] but is now extended to strong focusing in the solid state.

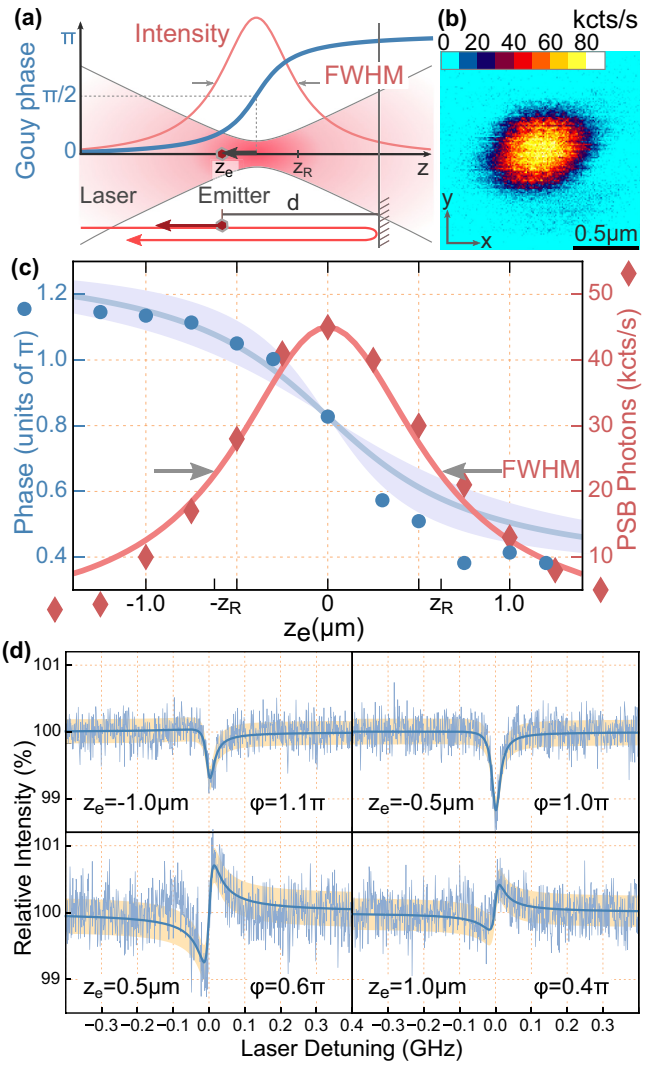

FIG. 3. Determination of the Gouy phase, utilizing the NV's E_x transition. (a) Optical focus (gray curve), intensity distribution (red curve), and Gouy phase (blue curve). (b) Lateral scan at the focus, $w_0 = 230\,\mathrm{nm}$. (c) The phase of the interference signal depends on the displacement of the emitter z_e. The phase change represents the Gouy phase. (d) Samples of the signal at different axial positions, z_e.

ACKNOWLEDGMENTS

We acknowledge the funding from the MPG, the SFB project CO.CO.MAT/TR21, the BMBF, the project Q.COM, and SQUTEC.

APPENDIX A: DATA COLLECTION

The measurements are performed with a home-built confocal setup using a Zeiss A-Plan, 40 ×, NA 0.65 objective. The NV center is contained in a 0.6-mm overgrown layer on the flat side of a macroscopic monolithic diamond solid immersion lens (SIL) [27]. The SIL resides inside a Janis bath cryostat SVT-400, operated in gas mode at 2 K.

The signals of APD1 and APD2 are simultaneously monitored, while the laser is detuned over a 1-GHz spectral range around the resonance frequency. Due to spectral diffusion of the NV center and an eventual drift of the scanning laser frequency, the collected signal does not have a constant frequency reference. To overcome this problem, for every scan, the phonon sideband signal is recorded and subsequently fitted with a Lorentzian line profile to determine the current resonance center of the frequency shift. Afterwards both signals, from APD1 and APD2, are shifted relative to the fitted center. Additionally during the measurement, the detuning range of the laser is corrected to symmetrically cover the last observed resonance center. The total signal is the sum of all these frequency-corrected single scans. Scans that do not meet the minimal fit criteria for linewidth (larger than 40–80 MHz or narrower than 10–30 MHz, depending on the excitation power) and amplitude (>40–100 cts/point or <3–20 cts/point, depending on the excitation power) or that show too large spectral jumps (100–200 MHz, depending on the excitation power), for example, after a repumping 532-nm laser pulse, are discarded.

APPENDIX B: DETECTED SIGNAL

The recorded signal is theoretically described as outlined in the following. The electric fields from the reflected laser $\mathbf{E}_\mathrm{L}$ as the local oscillator and from the emitter $\mathbf{E}_\mathrm{e}$ arrive on a detector in the far field and cause the total detected field

$$\mathbf{E}_\mathrm{det} = \mathbf{E}_\mathrm{L} + \mathbf{E}_\mathrm{e} e^{i\varphi}, \tag{B1}$$

where $\varphi = \varphi_\nu + \varphi_\mathrm{G} + \varphi_\mathrm{d}$ is the phase difference resumed from the phase lag $\varphi_\nu = \pi/2$ of the driven harmonic oscillator, the Gouy phase φ_G, and the phase delay φ_d caused by the different path lengths of the laser and the emitted photons.

The detected intensity is

$$\left\langle \mathbf{E}_\mathrm{det}^2 \right\rangle = \langle (\mathbf{E}_\mathrm{L} + \mathbf{E}_\mathrm{e} e^{i\varphi})^2 \rangle \tag{B2}$$

$$= \left\langle \mathbf{E}_\mathrm{L}^2 \right\rangle + \left\langle \mathbf{E}_\mathrm{e}^2 \right\rangle + 2\langle \mathbf{E}_\mathrm{L} \cdot \mathbf{E}_\mathrm{e} e^{i\varphi} \rangle. \tag{B3}$$

The intensity at the detector, dependent on the laser detuning Δ from the emitter resonance, can be expressed as

$$I_\mathrm{det} = I_\mathrm{L} + I_\mathrm{e}(\Delta) + 2\mathrm{Re}\{\mathbf{E}_\mathrm{L} \cdot \mathbf{E}_\mathrm{e} e^{i\varphi}\}. \tag{B4}$$

The first term is the reflected laser intensity I_L, which contributes to a constant background through the detuning range. The second term is the collected emission from the emitter I_e and has a Lorentzian line shape,

$$I_\mathrm{e}(\Delta) = C_\mathrm{e} \frac{\Gamma_2^2}{\Delta^2 + \Gamma_\mathrm{eff}^2}, \tag{B5}$$

where C_e is a coefficient proportional to the laser intensity and $\Gamma_\mathrm{eff} = \sqrt{\Gamma_2^2 + \frac{\Gamma_2}{\Gamma_1}\Omega^2}$ is the effective half-linewidth at the excitation power Ω^2.

The third term is the interference, I_intf, of the laser field and the emitter field:

$$I_\mathrm{intf} = 2\mathrm{Re}\{\mathbf{E}_\mathrm{L} \cdot \mathbf{E}_\mathrm{e} e^{i\varphi}\} \tag{B6}$$

$$= 2\mathrm{Re}\left\{ E_\mathrm{L} \cdot E_\mathrm{e} \frac{\Gamma_2 e^{i\varphi}}{\Delta + i\Gamma_\mathrm{eff}} \right\} \tag{B7}$$

$$= 2\sqrt{I_\mathrm{L} I_\mathrm{e}}\mathrm{Re}\left\{ \frac{\Gamma_2 e^{i\varphi}(\Delta + i\Gamma_\mathrm{eff})}{\Delta^2 + \Gamma_\mathrm{eff}^2} \right\} \tag{B8}$$

$$= 2\sqrt{I_\mathrm{L} I_\mathrm{e}} \frac{\Gamma_2 \Delta \cos\varphi + \Gamma_2 \Gamma_\mathrm{eff} \sin\varphi}{\Delta^2 + \Gamma_\mathrm{eff}^2}. \tag{B9}$$

Other than in the second term, the interference term contains only the coherent part of the emission field. The degree of coherence at resonance decreases proportionally with the power-broadened linewidth. Both coherent parts at off-resonant and resonant frequency are linear to the excitation field. A detailed treatment can be found, e.g., in [37]. The interference term is then modified to [22,38]

$$I_\mathrm{intf} = 2\sqrt{I_\mathrm{L} C_\mathrm{coh}} \frac{\Gamma_2 \Delta \cos\varphi + \Gamma_2^2 \sin\varphi}{\Delta^2 + \Gamma_\mathrm{eff}^2}, \tag{B10}$$

where C_coh is the coefficient proportional to the laser intensity. The coherent intensity at resonance is calculated as

$$I_\mathrm{coh} = \left\langle \mathbf{E}_\mathrm{coh}^2 \right\rangle \tag{B11}$$

$$= C_\mathrm{coh} \frac{\Gamma_2^2 \left(\Delta^2 + \Gamma_2^2\right)}{\left(\Delta^2 + \Gamma_\mathrm{eff}^2\right)} \tag{B12}$$

$$\underset{\Delta=0}{=} C_\mathrm{coh} \frac{\Gamma^4}{\Gamma_\mathrm{eff}}. \tag{B13}$$

Due to the weak ZPL, the total ZPL emission I_e is expected to be very small in comparison to the interference effect. The total signal on the detector is therefore

$$I_\mathrm{det} \approx I_\mathrm{L} + I_\mathrm{intf} \tag{B14}$$

$$= I_\mathrm{L} + 2\sqrt{I_\mathrm{L} C_\mathrm{coh}} \frac{\Gamma_2 \Delta \cos\varphi + \Gamma_2^2 \sin\varphi}{\Delta^2 + \Gamma_\mathrm{eff}^2} \tag{B15}$$

$$= I_\mathrm{L}\left(1 + 2\sqrt{\frac{C_\mathrm{coh}}{I_\mathrm{L}}} \frac{\Gamma_2 \Delta \cos\varphi + \Gamma_2^2 \sin\varphi}{\Delta^2 + \Gamma_\mathrm{eff}^2}\right). \tag{B16}$$

APPENDIX C: COHERENT PHOTONS

To determine the amount of coherent photons, which depends on the excitation power, first we determine the saturation parameter S, based on the PSB fluorescence intensity I_PSB, which is proportional the total emission I:

$$S = \frac{I}{I_\mathrm{sat} - I}. \tag{C1}$$

The saturation intensity I_{sat} and the homogeneous linewidth $2\Gamma_2$ can be deduced from the dependency of the effective linewidth $2\Gamma_{\text{eff}}$ on the total emission [Fig. 2(a)]:

$$\Gamma_{\text{eff}} = \Gamma_2\sqrt{\frac{I_{\text{sat}}}{I_{\text{sat}} - I}}. \tag{C2}$$

The parameters are fitted to $2\Gamma_2 = 26.2$ MHz and $I_{\text{sat}} = 95$ kcts/s.

The total intensity [Fig. 2(b)] can than expressed by the saturation parameter. Since S is defined by the measured values of I, the measured points match perfectly on the theoretical curve:

$$I = I_{\text{sat}}\frac{S}{S+1}. \tag{C3}$$

The coherent part of the scattered light can be expressed by the lifetime-limited linewidth Γ_1, the homogeneous linewidth $2\Gamma_2$, and the saturation parameter S. Additionally, in the interference measurement, the detection efficiency and the mode overlapping with the reflected laser beam add a constant factor $\eta \ll 1$ to the equation:

$$I_{\text{coh}} = \eta\frac{\Gamma_1^2}{4\Gamma_2}\frac{S}{(S+1)^2} \tag{C4}$$

$$= I_{\text{coh}}^{\max}\frac{4S}{(S+1)^2}. \tag{C5}$$

In theory the amount of coherent photons reaches the maximum at $S = 1$ according to the gray curve in Fig. 2(b). The maximal amount of coherent photons $I_{\text{coh}}^{\max}$ is one-fourth of the total resonant emission I_{total}. I_{total} can be estimated from the Debye-Waller factor $\alpha_{\text{DW}} \approx 4\%$ and the PSB emission $I_{\text{sat}} \approx 95$ kcts/s:

$$I_{\text{coh}}^{\max} = I_{\text{coh},S=1} = \tfrac{1}{4}I_{\text{total}} \tag{C6}$$

$$= \tfrac{1}{4}\cdot 0.04 \cdot 95 \text{ kcts/s} \tag{C7}$$

$$= 950 \text{ cts/s}. \tag{C8}$$

The narrow-band filter (BP2) has a transmission of 60%, so the number of coherent photons is reduced to ≈600 cts/s. The measured data show an additional decoherence behavior, which leads to a modification in the theoretical prediction:

$$I_{\text{coh}} = I_{\text{coh,meas}}^{\max}\frac{4S}{(S+1)^2}\frac{1}{\exp(S/1.3)}. \tag{C9}$$

The ratio between coherent and total emission $I_{\text{coh}}/I\text{tot}$ follows this modification as shown in Fig. 2(c):

$$\frac{I_{\text{coh}}}{I_{\text{tot}}} = \eta\frac{1}{S+1}\frac{1}{\exp(S/1.3)}. \tag{C10}$$

The factor $S/1.3$ expresses the relative incoming laser power P_{in} in terms of the specific saturated power of the environment $P_{\text{env}} = 4.0$ nW. So the terms above originate from

$$I_{\text{coh}} = I_{\text{coh,meas}}^{\max}\frac{4S}{(S+1)^2}\frac{1}{\exp(P_{\text{in}}/P_{\text{env}})}, \tag{C11}$$

$$\frac{I_{\text{coh}}}{I_{\text{tot}}} = \xi\frac{1}{S+1}\frac{1}{\exp(P_{\text{in}}/P_{\text{env}})}. \tag{C12}$$

The exponential reduction in the coherent scattering depending on the excitation power can be explained as the effect of charge fluctuation in the near environment due to laser illumination. The NV center is embedded in a lattice with many other fluorescent and nonfluorescent defects. In general, charge noise causes spectral diffusion, which is expressed in the linewidth broadening. Charge deposition during the time in the excited state furthermore leads to frequency fluctuation and hence decoherence of the emitted photons. Since the wide-band collection of the PSB is not affected by the coherence, the PSB signal does not suffer from the charge effect.

In the experiment, even without a charge noise effect, at most 26 coherent photons per second were observed. This means a factor of $1/\xi = I_{\text{coh}}^{\max}/I_{\text{coh,meas}}^{\max} = 23$ less than the expected 650 coherent photons per second calculated based on the PSB emission. This can be explained by the imperfect mode matching of the emitter to the laser.

APPENDIX D: ABSORPTION CROSS SECTION

The theoretical absorption cross section σ_{abs} and the associated absorption diameter $\varnothing$ of the NV center is determined by the Debye-Waller factor α_{DW} and the absorption wavelength λ:

$$\sigma_{\text{abs}} = \alpha_{\text{DW}}\frac{\Gamma_1}{2\Gamma_2}\frac{3\lambda^2}{2\pi} \tag{D1}$$

$$= 0.04\frac{13 \text{ MHz}}{26 \text{ MHz}}\frac{3\cdot 0.637^2}{2\pi}\ \mu\text{m}^2 \tag{D2}$$

$$\approx 0.04 \cdot 0.5 \cdot 0.194\ \mu\text{m}^2 = 3875 \text{ nm}^2, \tag{D3}$$

$$\varnothing_{\text{abs}} \approx 70 \text{ nm}. \tag{D4}$$

From the extinction visibility $\mathcal{V}$ and laser focus spot $A = \pi w_0^2 = \pi\cdot(0.23\ \mu\text{m})^2 = 0.166\ \mu\text{m}^2$, one can estimate these quantities as (Table I)

$$\mathcal{V}_{\text{cal}} = \frac{\sigma_{\text{abs}}}{A} = 2.3\%, \tag{D5}$$

$$\varnothing = 2\sqrt{\frac{\sigma}{\pi}} = 2\sqrt{\frac{\mathcal{V}A}{\pi}} = 2\sqrt{\frac{\mathcal{V}\pi w_0^2}{\pi}} \tag{D6}$$

$$= 2w_0\sqrt{\mathcal{V}} = 0.46\sqrt{\mathcal{V}}\ \mu\text{m}, \tag{D7}$$

$$\sigma = \mathcal{V}A. \tag{D8}$$

The cross section can be estimated for different cases, including where all reflected laser light is collected (1000× laser, that is, $1/\sqrt{1000}$ of the measured visibility) and also all

TABLE I. Measured and calculated absorption cross-sections for a single NV-center.

	Calculated (FW)	Measured (BW)	1000 × laser	1000 × laser, 23 × coherent
Visibility $\mathcal{V}$	2.3%	2.8%	0.09%	0.42%
ϕ	70 nm	77 nm	14 nm	30 nm
σ	3875 nm^2	4650 nm^2	147 nm^2	706 nm^2

coherent photons interfere (1000× laser, 23× coherent, that is, $\sqrt{23/1000}$ of the measured visibility)

APPENDIX E: GOUY PHASE

Other than in a transmission measurement, the signal of the interference in the reflection experiences an arbitrary phase:

$$\varphi = \varphi_v + \varphi_G + \varphi_\mathrm{d}. \tag{E1}$$

The first term rises from the lag of the driven oscillator and is $\pi/2$ at resonance. The second term is the Gouy phase of the focused laser beam at the position of the emitter. For an optimal placement of the emitter at the beam focus, this term contributes to a phase difference of $\pi/2$ between the emitter and the laser beam in the far field. The third term rises from the additional path of the laser, reflected back from interfaces, in this experiment mainly from the diamond-vacuum interface behind the emitter. Since the emitter in this case is embedded in the solid-state dielectric, the phase φ_d is specific by the distance d to the reflection interface and the refractive index of the dielectric n:

$$\varphi_\mathrm{d} = 2\pi(2dn \bmod \lambda). \tag{E2}$$

In experiments, for an optimal coupling and collection efficiency, the emitter is placed directly in the focus of the laser beam. In general, the emitter picks up the phase of the laser beam right at its location. It can also be placed in different locations as a probe to monitor the phase of the laser beam at these places. By moving the emitter axially, the change in the Gouy phase φ_G can be measured.

The Gouy phase of a laser beam with the focus at $z = 0$ is

$$\phi_G(z) = \frac{\pi}{2} + \arctan\left(\frac{z}{z_R}\right); \tag{E3}$$

here z_R denotes the Rayleigh length of the beam, defined by the refractive index n, the beam waist w_0, and the wavelength λ:

$$z_R = \frac{n\pi w_0^2}{\lambda}. \tag{E4}$$

By placing the emitter at z_e, the emitted field adapts the phase at this place and evolves with this phase to the far field. On the contrary, the laser field continuously gains phase according to the Gouy phase:

$$\phi_\mathrm{e}(z=\infty) = \phi_G(z_\mathrm{e}), \tag{E5}$$

$$\phi_\mathrm{L}(z=\infty) = \frac{\pi}{2}. \tag{E6}$$

The total detected phase shift in the far field due to the Gouy phase is then

$$\varphi_G(z_\mathrm{e}) = \phi_\mathrm{L}(z=\infty) - \phi_\mathrm{e}(z=\infty) \tag{E7}$$

$$= \frac{\pi}{2} - \phi_G(z_\mathrm{e}). \tag{E8}$$

The total detected phase becomes

$$\varphi(z_\mathrm{e}) = \varphi_v + \varphi_\mathrm{d} - \varphi_G(z_\mathrm{e}) \tag{E9}$$

$$= \varphi_0 - \varphi_G(z_\mathrm{e}). \tag{E10}$$

In the experiment, by placing the emitter perfectly in the laser focus, the signal exhibits a phase of $\varphi_0 = 0.86\pi$. By displacing the z scanner out of focus, different phases, depending on the axial position, are measured:

$$\phi_G(z_\mathrm{e}) = \frac{\pi}{2} - \varphi_0 + \varphi_G(z_\mathrm{e}). \tag{E11}$$

For the theoretical curve, a beam waist of $w_0 = 0.23\ \mu$m is applied. The waist is obtained from the lateral scan in Fig. 3(b). This corresponds to a Rayleigh length of $z_R = 0.62\ \mu$m. We assume an error bar of $\pm 0.05\ \mu$m due to the inaccuracy of the piezo-scanner to define the lower and upper bounds for the beam waist as 0.18 and 0.28 μm. The resulting Rayleigh lengths are 0.38 and 0.92 μm, respectively. These provided the tolerance band in Fig. 3(c).

The peak power of the Gaussian beam depends on the axial displacement and is

$$I(z) = I_0 \frac{1}{1 + (z/z_\mathrm{R})^2}, \tag{E12}$$

which fits the measured intensity very well. Here the saturation effect and the decreasing collection efficiency out of focus are neglected, since they have the opposite effect on the intensity.

APPENDIX F: EFFECT OF NONINTERFERING PHOTONS

In the text, we assume that the emission intensity into the ZPL and the leakage from the PSB are negligible for the interference measurement. This is based on the fact that the coherent interfering field is amplified by the strong laser field, while the noninterfering intensity scales with the square of the coherent emitted field, which, in the case of the NV center, is very weak in comparison with the laser field. To examine this assumption, the signal is analyzed dependent on the polarization.

The interference signal can be decomposed into the dispersive $\mathcal{D}$ and the absorptive Lorentzian $\mathcal{L}$ parts,

$$I_\mathrm{intf} = 2\sqrt{C_\mathrm{coh} I_\mathrm{L}} \frac{\Gamma_2 \Delta \cos\varphi + \Gamma_2^2 \sin\varphi}{\Delta^2 + \Gamma_\mathrm{eff}^2} \tag{F1}$$

$$= 2\sqrt{C_\mathrm{coh} I_\mathrm{L}} (\mathcal{D}(\Delta)\cos\varphi + \mathcal{L}(\Delta)\sin\varphi), \tag{F2}$$

with

$$\mathcal{D}(\Delta) = \frac{\Gamma_2 \Delta}{\Delta^2 + \Gamma_\mathrm{eff}^2}, \quad \mathcal{L}(\Delta) = \frac{\Gamma_2^2}{\Delta^2 + \Gamma_\mathrm{eff}^2}. \tag{F3}$$

In addition, the leaking from the PSB I_PSB and the emission intensity at ZPL I_e also exhibit the Lorentzian line shape,

$$(I_\mathrm{e} + \epsilon I_\mathrm{PSB})\mathcal{L}(\Delta) = I_\mathrm{inc}\mathcal{L}(\Delta), \tag{F4}$$

where ϵ introduces the possible small leaking ratio.

To separate these terms, the excitation and the analyzing polarizations are now rotated out of the NV dipole axis. The NV polarization is rotated to the angle α and the analyzing polarization is at the angle θ with respect to the laser polarization (Fig. 4). The angle α is set by the half-wave plate in front of the cryostat; the polarization angle θ, by the polarizer (Pol2) in front of the single-photon detector (APD2).

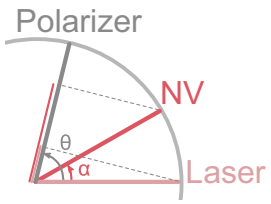

FIG. 4. Polarization configuration. The angle between the excitation laser and the NV dipole is set to α. The polarizer (Pol2; in front of the detector, APD2) is varied to select the analyzing angle θ. On the detector, only the projections of the NVs and the linear polarized laser fields on the polarizer axis are measured.

The angle θ does not affect the photon fields going out from the cryostat, but only projects them onto the axis of the polarizer. By rotating the detection polarization θ, the emitter field evolves with $\cos(\theta-\alpha)$, while the laser field evolves with $\cos\theta$:

$$E_{\mathrm{L}} \rightarrow E_{\mathrm{L}}\cos\theta, \tag{F5}$$

$$E_{\mathrm{e}} \rightarrow E_{\mathrm{e}}\cos(\theta-\alpha). \tag{F6}$$

The total signal depends on θ as

$$I_{\mathrm{det}} = I_0 + (2\sqrt{C_{\mathrm{coh}}I_{\mathrm{L}}}\cos\theta\cos(\theta-\alpha)\cos\varphi\mathcal{D}(\Delta) \tag{F7}$$

$$+ (2\sqrt{C_{\mathrm{coh}}I_{\mathrm{L}}}\cos\theta\cos(\theta-\alpha)\sin\varphi\mathcal{L}(\Delta) \tag{F8}$$

$$+ I_{\mathrm{inc}}\cos^2(\theta-\alpha)\mathcal{L}(\Delta). \tag{F9}$$

The dispersive part with amplitude $\mathcal{M}$ is not affected by the incoherent photons, while the absorptive amplitude $\mathcal{N}$ also includes these:

$$\mathcal{M} = 2\sqrt{C_{\mathrm{coh}}I_{\mathrm{L}}}\cos\theta\cos(\theta-\alpha)\cos\varphi, \tag{F10}$$

$$\mathcal{N} = 2\sqrt{C_{\mathrm{coh}}I_{\mathrm{L}}}\cos\theta\cos(\theta-\alpha)\sin\varphi + I_{\mathrm{inc}}\cos^2(\theta-\alpha). \tag{F11}$$

As illustrated in Fig. 5, the incoherent intensity eventually modifies the amplitude $\mathcal{N}$, so that the ratio of $\mathcal{M}$ and $\mathcal{N}$ is changed. Note that the interference angle φ is determined from the signal as $\tan^{-1}(\mathcal{N}/\mathcal{M})$, so that it was not possible to definitively determine φ and I_{inc} from the polarization-independent measurement.

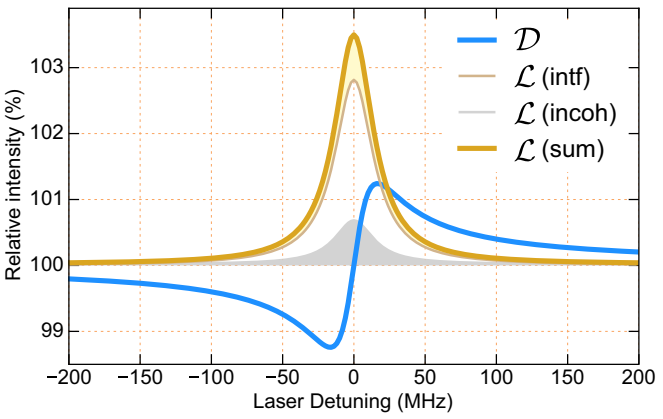

FIG. 5. Decomposition of the interference signal into the dispersive part $\mathcal{D}$ and the Lorentzian part $\mathcal{L}$. The effective Lorentzian part $\mathcal{L}$ (sum) includes the interfered Lorentzian $\mathcal{L}$ (intf) and the noninterfered Lorentzian part $\mathcal{L}$ (incoh).

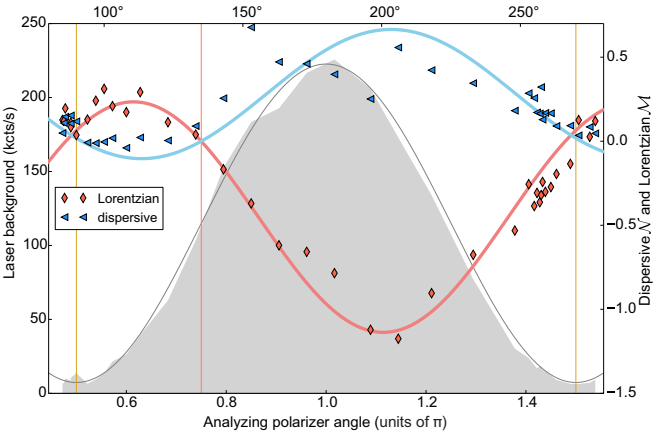

FIG. 6. Evolution of the amplitudes $\mathcal{M}$ and $\mathcal{N}$ depends on the detection angle θ in the laser frame. The gray curve represents the laser background, which vanishes at $\theta=\pi/2$ (yellow line). The red line indicates $\theta=\pi/2+\alpha$, where the NV emission vanishes.

By determining $\mathcal{M}$ and $\mathcal{N}$ for a varying θ, the effect of I_{inc} can be extracted. As shown in Fig. 6, $\mathcal{M}$ and $\mathcal{N}$ can be fitted well with $\cos\theta\cos(\theta-\alpha)$. An effect of I_{inc} would appear at $\theta=\pi/2$. Here, since the laser is crossed out, no interference signal is expected and only I_{inc} should remain in $\mathcal{N}$. As we can see, $\mathcal{N}$ and $\mathcal{M}$ are well proportional over all the angles, and at $\theta=\pi/2$, $\mathcal{N}$ is below the noise level. So we can assume that the effect of noninterfering photons is negligible in comparison to the measurement noise.

APPENDIX G: VISIBILITY AND SIGNAL-TO-NOISE RATIO

1. Dependence on the saturation parameter

The effective visibility of the signal or contrast $\mathcal{C}$ at resonance depends on the ratio between the coherent photons and the laser excitation intensity. At low excitation, the contrast $\mathcal{C}$ reaches its maximum value, which is equal to $\mathcal{V}$, which is specific for every emitter in the experiment. With Eq. (B16) for $\Delta=0$ and $\sin\varphi=1$, the contrast $\mathcal{C}$ can be written as

$$\mathcal{C} = 2\sqrt{\frac{C_{\mathrm{coh}}}{I_{\mathrm{L}}}}\frac{\Gamma_2^2}{\Gamma_{\mathrm{eff}}^2}, \tag{G1}$$

$$\mathcal{C}(S) \propto \frac{1}{S+1}. \tag{G2}$$

Note that the intensity in the ZPL of the NV centers I_{e} is much weaker than the laser background I_{L}, so that the interference effect dominates. Therefore, the contrast can be referenced to the laser background I_{L} instead of to the signal at resonance $I_{\mathrm{L}}+I_{\mathrm{e}}$ ($\Delta=0$).

We calculate the maximal signal-to-noise ratio achieved at the shot-noise limit. The relative shot noise $\mathcal{N}$ is defined by the laser background, which is proportional to the excitation power. The relative shot noise can then be expressed by the

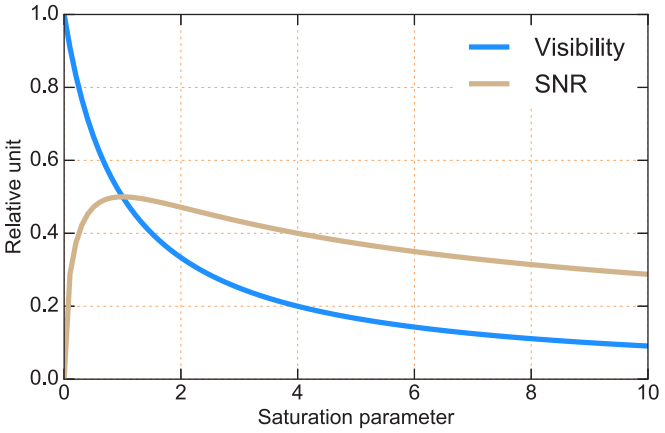

FIG. 7. The visibility and SNR depend on the saturation power.

saturation parameter S,

$$\mathcal{N} \propto \frac{1}{\sqrt{S}}, \tag{G3}$$

which leads to the expression for the SNR:

$$\mathrm{SNR} = \frac{\mathcal{V}}{\mathcal{N}} \propto \frac{\sqrt{S}}{S+1}. \tag{G4}$$

The trend of the visibility and the SNR is shown in Fig. 7. While the visibility decreases with higher excitation power, the shot noise decreases. At the result, the best SNR for the extinction signal should be achieved at $S = 1$. However, the additional reduction in the coherent photons due to charge noise reduces the coherence, so that in the presented experiment, the maximal SNR is reached at $S = 0.45$.

2. Dependence on the polarization cross-angle

In the cross-polarization configuration, the excitation power S and excitation angle α are set constant. The intensity of the laser and the emission are set by the polarizer in front of the detector APD2. The visibility is modified from Eq. (G2)

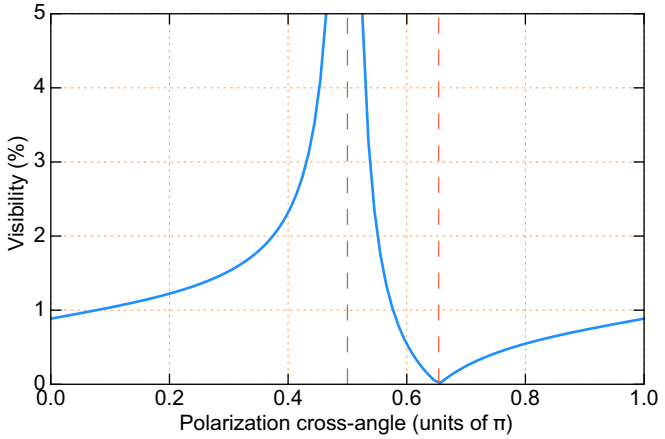

FIG. 8. Visibility in the cross-polarization configuration. At 0.5π (dashed gray vertical line) the laser is perpendicular to the detection polarization. At the dashed red vertical line, the emitter is perpendicular to the detection polarization.

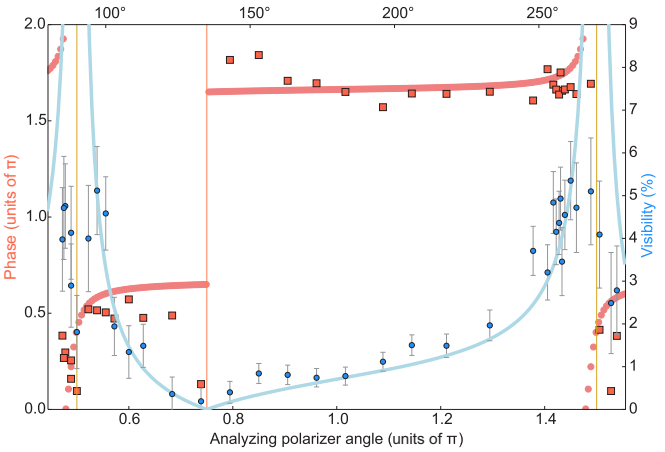

FIG. 9. Phase and visibility depend on the detection polarization. Yellow lines ($\pi/2$ and $3\pi/2$): the laser is perpendicular to the detection polarization. Red line: the NV is perpendicular to the detection polarization.

according to the polarizer angle θ:

$$\mathcal{V}(\theta) \propto \frac{\cos(\theta - \alpha)}{\cos\alpha}. \tag{G5}$$

The trend of $\mathcal{V}(\theta)$ is shown in Fig. 8. At cross-angle $\theta = \pi/2$, the laser polarization is perpendicular to the polarizer and therefore completely blocked, while the emitter's photons are still present. Hence the visibility increases near this angle. At the other featured angle (dashed red line), the NV emission is completely crossed out, so even with the remaining laser background, no interference occurs.

Figure 9 shows that the visibility and the phase depend on the polarization configuration. The visibility evolves as expected. Near the laser-crossed point, the visibility increases; concurrently the noise level rises up because of the weak laser background. Additionally, the degree of laser polarization is

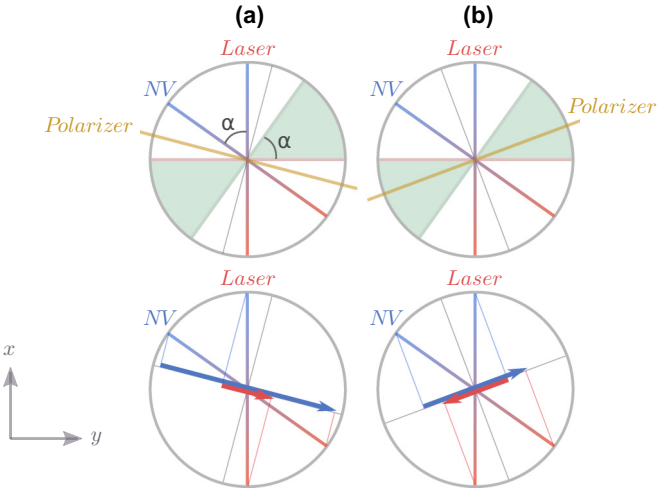

FIG. 10. Phase flip of π due to the geometrical configuration. (a) The polarizer lies in the "normal" area; the phase between the projected dipoles on the polarizer is unchanged. (b) The polarizer lies in the "abnormal" area; the projected dipoles oscillate in counter-phase to each other, adding an additional phase of π.

not unity. As a result, the visibility at this point lies below the fitted expected value.

The phase of the signal is not constant for all analyzing polarization angles. A phase flip by π can be observed at the polarization angles, where either the laser light or the NV's emission is crossed out. This is a geometrical configuration effect, as illustrated in Fig. 10. The analyzing polarization can lie in different angular areas defined by the perpendicular lines to the laser and to the NV's dipole. On the polarizer axis, the projection of the laser and the NV dipole can be in-phase or antiphase with each other. The abnormal sector, the angular area, where the projection becomes antiphase, has the angular extent of the angle between the laser and the NV's dipole α.

[1] G. Balasubramanian, I. Y. Chan, R. Kolesov, M. Al-Hmoud, J. Tisler, C. Shin, C. Kim, A. Wojcik, P. R. Hemmer, A. Krueger *et al.*, Nature **455**, 648 (2008).

[2] T. Staudacher, F. Shi, S. Pezzagna, J. Meijer, J. Du, C. A. Meriles, F. Reinhard, and J. Wrachtrup, Science **339**, 561 (2013).

[3] P. Neumann, J. Beck, M. Steiner, F. Rempp, H. Fedder, P. R. Hemmer, J. Wrachtrup, and F. Jelezko, Science **329**, 542 (2010).

[4] G. Waldherr, Y. Wang, S. Zaiser, M. Jamali, T. Schulte-Herbruggen, H. Abe, T. Ohshima, J. Isoya, J. F. Du, P. Neumann *et al.*, Nature **506**, 204 (2014).

[5] F. Dolde, I. Jakobi, B. Naydenov, N. Zhao, S. Pezzagna, C. Trautmann, J. Meijer, P. Neumann, F. Jelezko, and J. Wrachtrup, Nat. Phys. **9**, 139 (2013).

[6] A. Sipahigil, M. L. Goldman, E. Togan, Y. Chu, M. Markham, D. J. Twitchen, A. S. Zibrov, A. Kubanek, and M. D. Lukin, Phys. Rev. Lett. **108**, 143601 (2012).

[7] F. Jelezko and J. Wrachtrup, Phys. Status Solidi **203**, 3207 (2006).

[8] S. Yang, Y. Wang, D. D. B. Rao, T. Hien Tran, A. S. Momenzadeh, M. Markham, D. J. Twitchen, P. Wang, W. Yang, R. Stöhr *et al.*, Nat. Photon. **10**, 507 (2016).

[9] H. Bernien, B. Hensen, W. Pfaff, G. Koolstra, M. S. Blok, L. Robledo, T. H. Taminiau, M. Markham, D. J. Twitchen, L. Childress *et al.*, Nature **497**, 86 (2013).

[10] B. Hensen, H. Bernien, A. E. Dreau, A. Reiserer, N. Kalb, M. S. Blok, J. Ruitenberg, R. F. L. Vermeulen, R. N. Schouten, C. Abellan *et al.*, Nature **526**, 682 (2015).

[11] A. Batalov, V. Jacques, F. Kaiser, P. Siyushev, P. Neumann, L. J. Rogers, R. L. McMurtrie, N. B. Manson, F. Jelezko, and J. Wrachtrup, Phys. Rev. Lett. **102**, 195506 (2009).

[12] R. J. Glauber, Phys. Rev. **131**, 2766 (1963).

[13] B. R. Mollow, Phys. Rev. **188**, 1969 (1969).

[14] H. J. Kimble, M. Dagenais, and L. Mandel, Phys. Rev. Lett. **39**, 691 (1977).

[15] D. J. Wineland, W. M. Itano, and J. C. Bergquist, Opt. Lett. **12**, 389 (1987).

[16] I. Gerhardt, G. Wrigge, P. Bushev, G. Zumofen, M. Agio, R. Pfab, and V. Sandoghdar, Phys. Rev. Lett. **98**, 033601 (2007).

[17] G. Wrigge, I. Gerhardt, J. Hwang, G. Zumofen, and V. Sandoghdar, Nat. Phys. **4**, 60 (2008).

[18] A. N. Vamivakas, M. Atatüre, J. Dreiser, S. T. Yilmaz, A. Badolato, A. K. Swan, B. B. Goldberg, A. Imamoglu, and M. S. Ünlü, Nano Lett. **7**, 2892 (2007).

[19] M. K. Tey, Z. Chen, S. A. Aljunid, B. Chng, F. Huber, G. Maslennikov, and C. Kurtsiefer, Nat. Phys. **4**, 924 (2008).

[20] C. Matthiesen, A. N. Vamivakas, and M. Atatüre, Phys. Rev. Lett. **108**, 093602 (2012).

[21] C. H. H. Schulte, J. Hansom, A. E. Jones, C. Matthiesen, C. Le Gall, and M. Atature, Nature **525**, 222 (2015).

[22] T. Plakhotnik and V. Palm, Phys. Rev. Lett. **87**, 183602 (2001).

[23] C. Cohen-Tannoujdi, J. Dupont-Roc, and G. Grynberg, *Atom-Photon Interactions: Basic Processes and Applications* (Wiley-VCH, Weinheim, 2011).

[24] G. Zumofen, N. M. Mojarad, V. Sandoghdar, and M. Agio, Phys. Rev. Lett. **101**, 180404 (2008).

[25] R. G. Newton, Am. J. Phys. **44**, 639 (1976).

[26] B. B. Buckley, G. D. Fuchs, L. C. Bassett, and D. D. Awschalom, Science **330**, 1212 (2010).

[27] P. Siyushev, F. Kaiser, V. Jacques, I. Gerhardt, S. Bischof, H. Fedder, J. Dodson, M. M. D. Twitchen, F. Jelezko, and J. Wrachtrup, Appl. Phys. Lett. **97**, 241902 (2010).

[28] J. R. Maze, A. Gali, E. Togan, Y. Chu, A. Trifonov, E. Kaxiras, and M. D. Lukin, New J. Phys. **13**, 025025 (2011).

[29] P. Siyushev, H. Pinto, M. Vörös, A. Gali, F. Jelezko, and J. Wrachtrup, Phys. Rev. Lett. **110**, 167402 (2013).

[30] L. G. Gouy, *Sur une propriété nouvelle des ondes lumineuses* (Gauthier-Villars, 1890).

[31] S. Feng and H. G. Winful, Opt. Lett. **26**, 485 (2001).

[32] J. Hwang and W. E. Moerner, Opt. Commun. **280**, 487 (2007).

[33] D. D. Bhaktavatsala Rao, S. Yang, and J. Wrachtrup, Phys. Rev. B **92**, 081301 (2015).

[34] W. J. Munro, K. Nemoto, and T. P. Spiller, New J. Phys. **7**, 137 (2005).

[35] G. Wrigge, J. Hwang, I. Gerhardt, G. Zumofen, and V. Sandoghdar, Opt. Express **16**, 017358 (2008).

[36] G. Hétet, L. Slodička, M. Hennrich, and R. Blatt, Phys. Rev. Lett. **107**, 133002 (2011).

[37] R. Loudon, *The Quantum Theory of Light* (Oxford University Press, New York, 2000).

[38] G. Wrigge, Ph.D. thesis, 2008, http://e-collection.library.ethz.ch/view/eth:31016.